JOURNAL OF MAGNETIC RESONANCE **133,** 330–340 (1998)
ARTICLE NO. MN981473

The Effect of Bulk Magnetic Susceptibility on Solid State NMR Spectra of Paramagnetic Compounds

Atsushi Kubo,[1] Thomas P. Spaniol,[2] and Takehiko Terao

Department of Chemistry, Graduate School of Science, Kyoto University, Kyoto 606-8502, Japan

Received October 6, 1997; revised March 18, 1998

The effect of bulk magnetic susceptibility (BMS) on solid state NMR spectra of paramagnetic compounds was investigated theoretically and experimentally. The BMS shift was calculated for cylindrical and spherocylinderical containers with some ratios of the length L and the diameter D. The results show the best resolution can be obtained by using a long cylindrical sample container with $L/D > 10$ and by exciting only the region near the center of the container. The effect of the random orientations and distributions of crystallites in a powder sample was also calculated according to a model proposed by Schwerk *et al.* [*J. Magn. Reson. A* 119, 157 (1996)] with removing the Fermi contact term from their model. Static and the magic-angle spinning ^{13}C NMR spectra were recorded on two paramagnetic compounds of $Ln(C_2D_5SO_4)_3 \cdot 8H_2O$ where Ln = Pr, Yb. The modified theory predicts the BMS broadening of the experimental spectra very well. © 1998 Academic Press

Key Words: **solid state NMR; bulk magnetic susceptibility shift; paramagnetic samples; polycrystalline sample.**

INTRODUCTION

Bulk magnetic susceptibility (BMS) of a sample produces a demagnetizing field and causes a shift of NMR resonance frequency (*1, 2*). This shift depends on the shapes of interface where magnetic susceptibility changes discontinuously and on the distances between the observed nuclei and the interface. The quantitative estimate of this field is an important issue in NMR imaging of lung tissue and trabecular bones (*3, 4*). In solid-state magic-angle spinning (MAS) NMR experiments, randomly distributed demagnetizing fields in a powder sample are known to cause broadening of resonance lines, if the bulk magnetic susceptibility tensor is anisotropic (*5, 6*). This effect has been known as the anisotropic bulk magnetic susceptibility (ABMS) effect. However, the demagnetizing field can also distort the spinning sideband pattern of a MAS NMR spectrum or the envelope of a static powder NMR spectrum and makes it difficult to determine the principal values of paramagnetic or chemical shift tensor accurately (*7–10*). It is due to the fact that the demagnetizing field or the so-called BMS shift is a tensorial interaction. This BMS effect can appear, even if the bulk magnetic susceptibility of a crystal is isotropic.

In a recent publication, a model was proposed to calculate the ABMS and the BMS effects on static and MAS NMR spectra of a powder sample (*10*). The theoretical values were compared with ^1H NMR spectra of small molecules absorbed on a diamagnetic zeolite. These ABMS and BMS effects are expected to be more significant in paramagnetic samples. In one of our previous studies, we have also encountered difficulties in simulating ^2H two-dimensional NMR spectra of a paramagnetic lanthanide compound and have attributed the reason for the error to the BMS effect (*11*). In the present study, the model proposed in Ref. (*10*) is reexamined by comparing it with experimental results on paramagnetic lanthanide ethylsulfates, for which single-crystal X-ray diffraction (*12*) and magnetic susceptibility (*13–15*) data are available and thus the theoretical calculation of the ABMS and the BMS effects are possible. We also consider the effect of shapes of sample containers. This effect has been known to affect the line shape of nuclear acoustic resonance of ^{183}W in a cylindrical single crystal tungsten metal specimen (*16*). Great attention has been also paid to this effect on the resolution of solution-state high-resolution NMR experiments (*17–19*). If the sample is diamagnetic, the BMS effect due to a sample container can be removed by MAS (*19*). However, for strong paramagnetic samples we will show here that this effect can appear as spinning sidebands of MAS NMR spectra. To measure paramagnetic shift tensors precisely or to observe the BMS shift due to sample inhomogeneity and investigate microstructures of inhomogeneous materials, this effect must be removed. We will discuss how to remove the BMS shift due to a sample container.

THEORY

The demagnetizing field $\delta\boldsymbol{H}(\boldsymbol{r})$ caused by a single uniformly magnetized region is given by the gradient of a magnetic scalar potential ϕ (*20*):

$$\delta\boldsymbol{H}(\boldsymbol{r}) = -\boldsymbol{\nabla}\phi(\boldsymbol{r}), \qquad [1]$$

[1] To whom correspondence should be addressed.

[2] On leave from the Institut für Anorganische Chemie und Analytische Chemie, Johannes Gutenberg-Universität Mainz, D-55099 Mainz, Germany.

1090-7807/98 $25.00

where

$$\phi(\boldsymbol{r}) = (1/4\pi)\int_S |\boldsymbol{r}_S - \boldsymbol{r}|^{-1}\boldsymbol{M}\cdot d\boldsymbol{a}(\boldsymbol{r}_S). \qquad [2]$$

$\boldsymbol{r}_S$ and $\boldsymbol{r}$ are a position on the surface of the magnetized region and a position where the field is calculated, respectively, $d\boldsymbol{a}$ is a surface vector directed outward. $\boldsymbol{M}$ is the magnetization inside the surface and is given by

$$\boldsymbol{M} \approx \hat{\chi}(S)\cdot\boldsymbol{H}_0, \qquad [3]$$

where $\hat{\chi}(S)$ is the volume susceptibility tensor within a surface S. If several magnetized regions exist, Eq. [2] has to be replaced by the sum of surface integrals. Equation [1] can be written in the following form:

$$\delta\boldsymbol{H} = -\hat{\nu}(\boldsymbol{r}, S)\cdot\hat{\chi}(S)\cdot\boldsymbol{H}_0, \qquad [4]$$

where $\hat{\nu}(\boldsymbol{r}, S)$ is a demagnetizing tensor. Its components $\nu_{\alpha\beta}(\boldsymbol{r}, S)$, $(\alpha, \beta = x, y, z)$ are given by

$$\nu_{\alpha\beta}(\boldsymbol{r}, S) = (1/4\pi)\partial/\partial r_\alpha\int_S |\boldsymbol{r}_S - \boldsymbol{r}|^{-1}da_\beta(\boldsymbol{r}_S)$$

$$= (1/4\pi)\int_S |\boldsymbol{r}_S - \boldsymbol{r}|^{-3}(r_{S\alpha} - r_\alpha)da_\beta(\boldsymbol{r}_S). \qquad [5]$$

The trace of a demagnetizing tensor $Tr\{\hat{\nu}\}$ does not depend on the shape of the surface S. Taking the origin at $\boldsymbol{r}$ and using Gauss's law, we obtain

$$Tr\{\hat{\nu}(\boldsymbol{r})\} = (1/4\pi)\int_S r_S^{-3}\boldsymbol{r}_S\cdot d\boldsymbol{a}$$

$$= (1/4\pi)\int_V \nabla\cdot(\boldsymbol{r}'/r'^3)dV' = \int_V \delta(\boldsymbol{r}')dV'. \qquad [6]$$

$Tr\{\hat{\nu}\}$ equals 1 when $\boldsymbol{r} = (0, 0, 0)$ is inside the volume V, and 0 when it is outside the volume V. The demagnetizing tensor is uniform and isotropic inside a sphere: the three principal values of $\hat{\nu}$ are given by $\nu_1 = \nu_2 = \nu_3 = \frac{1}{3}$ (*20*). Outside the sphere, $\hat{\nu}$ represents the field produced by a dipole located at the center of the sphere:

$$\hat{\nu}(\boldsymbol{r}) = (V/4\pi)\{1/r^3 - 3\boldsymbol{r}'\boldsymbol{r}/r^5\}, \qquad [7]$$

where V is the volume of the sphere and the origin of $\boldsymbol{r}$ is the center of the sphere. For the surface with a general shape, the demagnetizing field must be calculated by a numerical integration of Eq. [5]. Analytical equations have been derived for a rectangular parallelepiped and a triangular surface (*3*, *4*).

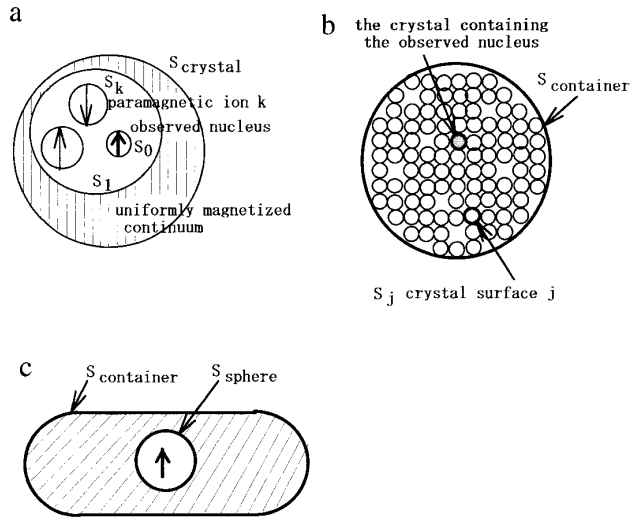

FIG. 1. Model of a polycrystalline sample. (a) Each crystallite is assumed to be spherical. We suppose a sphere S_0 with an infinitesimal radius which encloses an observed nucleus. If there is a finite distribution of unpaired electron spins on the nucleus, the magnetic susceptibility in S_0, $\hat{\chi}(S_0)$, is nonzero. S_1 is the Ewald sphere with a radius which is much smaller than the size of the crystallite, but large enough so that the average over lattice points converges. Inside the sphere S_1, the magnetization due to unpaired electrons is assumed to be localized in the spheres S_k $(k = 1, 2, \cdots)$, where S_k encloses the kth paramagnetic metal ion. The magnetic susceptibility inside S_k is given by $\hat{\chi}(S_k) = \hat{\chi}_k^{\text{ion}}/V_{\text{M}}$, where $\hat{\chi}_k^{\text{ion}}$ is the susceptibility of the kth paramagnetic ion, and V_{M} is the volume of S_k. The magnetic susceptibility of the region outside S_0 and S_k and inside S_1 is assumed to be zero: $\hat{\chi}(S_1) = 0$. The region outside S_1 and inside the crystallite S_{crystal} is assumed to be uniformly magnetized with the volume susceptibility $\hat{\chi}_{\text{V}} = (V_{\text{unit cell}})^{-1}\ \Sigma_{k\,\in\text{unit cell}}\ \hat{\chi}_k^{\text{ion}}$. (b) Spherical crystallites with the same radius are assumed to form a face-centered cubic lattice in a spherical container with a vacancy ratio $(1 - p)$. The magnetic susceptibility tensor of each crystallite is assumed to be randomly oriented. (c) In the sample container, we suppose a sphere which contains an observed nucleus. The magnetic susceptibility outside this sphere but within the container is assumed to be uniform and isotropic.

We consider a model of a polycrystalline sample proposed in Ref. (*10*). We assume that the polycrystalline sample can be divided to homogeneously magnetized regions as shown in Fig. 1. Spherical crystallites with an identical diameter are assumed to occupy lattice positions of a FCC structure with a probability p (Fig. 1b). In addition to their model, we place an infinitesimal sphere S_0 around an observed nucleus (Fig. 1a) and consider the effect of a sample container (Fig. 1c). The NMR resonance frequency at a position $\boldsymbol{r}$ inside a sample is proportional to the magnetic induction:

$$\boldsymbol{B}_{\text{in}} = \mu_0\{\boldsymbol{H}_0 + \boldsymbol{M} + \delta\boldsymbol{H}\}$$

$$= \mu_0\{1 + \hat{\chi}(S_0) - \sum_i \hat{\nu}(\boldsymbol{r}, S_i)\cdot\hat{\chi}(S_i)\}\boldsymbol{H}_0, \qquad [8]$$

where the sum is over all the regions shown in Fig. 1. One can define a shift tensor as

$$\hat{\delta}(\boldsymbol{r}) = \hat{\chi}(S_0) - \sum_i \hat{\nu}(\boldsymbol{r}, S_i)\hat{\chi}(S_i). \quad [9]$$

This shift tensor includes the Fermi contact term,

$$\hat{\delta}_{\text{con}} = \tfrac{2}{3}\,\hat{\chi}(S_0), \quad [10]$$

and the paramagnetic dipolar shift term,

$$\hat{\delta}_{\text{dip}} = (1/4\pi) \sum_{k \in S_1} \{3\boldsymbol{r}_k^t \boldsymbol{r}_k / r_k^5 - 1/r_k^3\}\hat{\chi}_k^{\text{ion}}, \quad [11]$$

where $\hat{\chi}_k^{\text{ion}}$ is the susceptibility tensor of the kth paramagnetic ion in S_1, and $\boldsymbol{r}_k$ is the vector from the observed nuclei to the kth paramagnetic ion. These two terms $\hat{\delta}_{\text{con}}$ and $\hat{\delta}_{\text{dip}}$ are determined by the molecular and crystal structures. The rest is defined as a BMS shift tensor, which depends on the packing of a polycrystalline sample or the shape of a sample container. The BMS shift tensor due to this polycrystalline effect is defined for a spherical sample container and is given by

$$\hat{\delta}_{\text{BMS}}^{\text{polycryst}}(\boldsymbol{r}) = (1/4\pi) \sum_j p_j[3(\boldsymbol{r}_j - \boldsymbol{r})({}^t\boldsymbol{r}_j - {}^t\boldsymbol{r})/|\boldsymbol{r}_j - \boldsymbol{r}|^5 - 1/|\boldsymbol{r}_j - \boldsymbol{r}|^3]\hat{\chi}_{\text{V}}^j V_{\text{cryst}}, \quad [12]$$

where $\boldsymbol{r}_j$ indicates the position of the center of the jth crystallite, $\hat{\chi}_{\text{V}}^j$ is the volume susceptibility of the jth crystallite, and V_{cryst} is the volume of the spherical crystallite. p_j is a random variable which takes 0 or 1, and the average of p_j over j corresponds to a packing probability p. The summation over j is taken for all the crystallites in a spherical sample container except the crystallite which contains the observed nucleus. In Ref. (*10*), the effect of this crystallite is also included in the BMS shift. However, our treatment shows that it should be included in the Fermi contact shift.

The effect of a container surface is defined as the deviation from a spherical container. We subtracted the spherical region which includes the observed nucleus from the sample container (see Fig. 1c). The magnetic susceptibility of the shaded region is assumed to be isotropic and is given by $\chi_{\text{V}}^{\text{iso,sample}}$. The BMS shift tensor is written as

$$\hat{\delta}_{\text{BMS}}^{\text{container}}(\boldsymbol{r}) = \chi_{\text{V}}^{\text{iso,sample}}\{1/3 - \hat{\nu}(\boldsymbol{r}, S_{\text{container}})\}. \quad [13]$$

In the above model of polycrystalline samples, the isotropic susceptibility is $\chi_{\text{V}}^{\text{iso,sample}} = 0.74p\chi_{\text{V}}^{\text{iso,cryst}}$, where $\chi_{\text{V}}^{\text{iso,cryst}}$ is an isotropic volume susceptibility of a individual crystallite and the factor 0.74 is the maximum packing density of a FCC lattice. $S_{\text{container}}$ is the outer surface of the sample container. If $S_{\text{container}}$ is a sphere, Eq. [13] is zero.

EXPERIMENTS

$Ba(C_2D_5SO_4)_2 \cdot 2H_2O$ was prepared according to the literature (*21*). Twenty milliliters of ethanol-d_6 were added to 18 ml of sulfuric acid with stirring and cooling and the solution was stirred for 2 days at 40°C. The solution was neutralized by adding $BaCO_3$ with cooling to 0°C and the precipitate of $BaSO_4$ was removed by centrifugation and filtration. White crystals precipitated when the solution was concentrated. Recrystallization from water gave 17 g of $Ba(C_2D_5SO_4)_2 \cdot 2H_2O$. Lanthanide ethylsulfates ($Ln(C_2D_5SO_4)_3 \cdot 8H_2O$, Ln = Pr, Yb) were prepared by stirring 5 g of the barium ethylsulfate with the corresponding amount of lanthanide sulfates in 20 ml of water (*22*). After removal of the precipitate of barium sulfate, the solution was concentrated by evaporation at room temperature to give the lanthanide compounds, which were purified by recrystallization from water.

All the ^1H and ^{13}C NMR experiments were performed at room temperature on a CMX300 spectrometer operating at 300.46 and 75.56 MHz for ^1H and ^{13}C, respectively, with a 7.5 mm ϕ spinner double resonance probe supplied from Chemagnetics. The RF field amplitude used for all the experiments was 50–60 kHz for both ^1H and ^{13}C.

As reported on europium acetate and sodium neodymium ethylenediaminetetraacetate (*23*), continuous-wave (CW) ^1H decoupling was found not to be effective to the lanthanide ethylsulfates because of the wide spread of ^1H resonance frequencies caused by the paramagnetic ions. The static ^{13}C NMR spectra of the lanthanide ethylsulfates were recorded under frequency-switched ^1H decoupling, whose frequency is switched every τ among three different ^1H offsets, $-f$, 0, and f, while the phase and the amplitude are kept constant. The time τ was fixed to the π-pulse length on resonance. The offset frequency f was chosen to maximize the amplitude of a Hahn echo observed under the frequency-switched decoupling. For the Pr compound, the echo amplitude became the largest at f = 50 kHz when the RF field strength was 60 kHz. For the Yb compound, no significant change of the echo amplitude was observed when f was varied. The transverse relaxation time T_2 was measured using the Hahn echo sequence under the frequency-switched ^1H decoupling. They were about 2 and 1 ms for the static powder samples of the Pr and Yb compounds, respectively. These values were about 100% and 10% longer than the T_2 in non-decoupling experiments. The CW ^1H decoupling gave T_2 values between those of the above two experiments.

We also measured T_2 of the Pr compound under MAS. They were in the following order: CW-decoupling (0.6 ms) < frequency-switched decoupling (7 ms) < non-decoupling (12 ms). Thus, we recorded MAS spectra without ^1H decoupling. In a normal MAS spectrum of the Yb compounds, the spinning

sidebands of the methyl and the methylene signals overlap severely. We used the five-pulse PASS sequence (*24, 25*) to separate sidebands with different orders.

RESULTS AND DISCUSSION

First we discuss the effect of a sample container on a static NMR spectrum. We consider here cylindrical and spherocylindrical containers with a length L and a diameter D; the spherocylinder with $L = D$ is a sphere. The angle between the cylinder axis and the static magnetic field is assumed to be the magic angle of 54.7°. We used a cylindrical coordinate fixed to the container and calculated the demagnetization tensor $\hat{\nu}(\boldsymbol{r}, S_{\text{container}})$ at $\boldsymbol{r} = (x\ 0\ z)$, where x and z are varied within the range of $0 \le x \le D/2$ and $-L/2 \le z \le L/2$. If $\boldsymbol{r}$ is in the xz-plane, the y-axis is one of the principal axes of $\hat{\nu}(\boldsymbol{r}, S_{\text{container}})$. Analytical solutions exist for the integration over the cylindrical axis z within the side plane of either a cylinder or a spherocylinder, as well as for the radial integration on the top and bottom planes of a cylinder (*16*), which are shown in Appendix A. The integrals over the other coordinates are calculated numerically. In Appendix B, we show that the demagnetizing tensor is symmetric for an arbitrary closed surface. The numerically calculated tensor $\hat{\nu}(\boldsymbol{r}, S_{\text{container}})$ was almost perfectly symmetric so that the error of the numerical integration must be sufficiently small.

In MAS NMR experiments, the static magnetic field is inclined by 54.7° from the cylinderical rotor axis, which is parallel to a Helmholtz coil. The unit vector parallel to the static field is given by $\mathbf{e}^h = (\sqrt{2/3}\cos\gamma, \sqrt{2/3}\sin\gamma, 1/\sqrt{3})$ in the coordinate system fixed to the cylinder. The BMS shift is given by

$$\delta_{\text{BMS}}^{\text{container,MAS}} = -\{C_1\cos\gamma + C_2\cos 2\gamma\}\chi_{\text{V}}^{\text{iso,sample}} \qquad [14a]$$

with

$$C_1 = \sqrt{2}/3(\nu_{xz} + \nu_{zx}) \qquad [14b]$$

$$C_2 = 1/3(\nu_{xx} - \nu_{yy}) \qquad [14c]$$

Figure 2 shows the contour plots of these coefficients C_1 and C_2 in a long cylinder ($L/D = 10$) and in an almost spherical spherocylinder with $L/D = 1.05$. The magnitudes of these coefficients are comparable in both containers and have the maximum values near the top and the bottom edges of the cylinder or near the side plane of the spherocylinder. Experimentally it is much easier to make a cylindrical sample container than a perfect spherical container. It is advisable to use a long cylindrical sample container for colloid and liquid crystalline samples and a long cylindrical crystal for single crystal experiments. However, for ordinary powder samples, the polycrystalline effect is much larger than the effect of a sample container. As is well known (*16–19*) and shown in Appendix A, the demagnetizing tensor is uniform in the xy-plane near the center ($z \cong 0$) of an infinitely long cylinder. When the cylindrical axis is inclined by the magic angle from the static magnetic field direction, this uniform shift is zero. Figures 2a and b show that the two coefficients C_1 and C_2 approach to zero when an observed position becomes apart from the top and bottom planes.

Figures 2a and b can be used to estimate the BMS shift due to a cylindrical container with an arbitrary L/D ratio less than 10. For example, the shift due to a container with $L/D = 4$ can be estimated from those in the region of $6 < z < 10$ in the figures. More than 50% of this sample region is affected by a BMS shift of magnitude less than $0.01\chi_{\text{V}}^{\text{iso,sample}}$. Figures 2a and b show that the BMS shift becomes large near the top and the bottom planes of the cylinder (*17–19*). It is shown in Appendix A that the coefficient C_1 diverges at the edge of the cylinder. If the whole region of a cylinder is observed, these regions yield broad components in static spectra and in spinning sidebands of MAS spectra. Such broadening can be removed, if the signal only from the central part of a cylinder is observed by using a susceptibility-matched glass spacer or a H_1 selective pulse (*26, 27*). The former technique is used in commercial sample tubes for high-resolution solution NMR, but is not popular for solid state NMR. For example, if the region more than $2.5D$ apart from the top and bottom planes is observed, the BMS shift is expected to be less than 10^{-3} $\chi_{\text{V}}^{\text{iso,sample}}$ from Figs. 2a and b.

To confirm the above results, we measured ^{1}H static and MAS NMR spectra of 1 M water solutions of $Dy(NO_3)_3 \cdot 9H_2O$ filled in cylindrical containers with some L/D values, and also calculated the spectra for the same sample configurations. The value of 590 ppm for the isotropic volume susceptibility of the sample, $\chi_{\text{V}}^{\text{iso,sample}}$, was used in the calculation, which was obtained by a free ion approximation (*28*). The results are shown in Fig. 3. The agreements between the experimental and the calculated spectra are satisfactory. The full width at half maximum (FWHM) of the experimental and the calculated static NMR spectra, which are expressed in the unit of $\chi_{\text{V}}^{\text{iso,sample}}$, are 3×10^{-2} and 6×10^{-2} for $L/D = 0.8$ (a) and (d), 7×10^{-3} and 3×10^{-3} for $L/D = 3.3$ (b) and (e), and 2.2×10^{-3} and 3×10^{-5} for $L/D = 12$ (c) and (f), respectively. The FWHM of the experimental spectrum (c) is much larger than the calculated value, while it is almost equivalent to the value 240 Hz calculated from the measured T_2 of 1.3 ms. The MAS NMR spectra of (a), (b), (d), and (e) show the spread of spinning sidebands which is similar to the envelope of the static spectra. A significant number of sidebands are observed even for a container with $L/D = 3.3$ (b). However, as shown later, the polycrystalline effect has the magnitude of $\delta_{\text{BMS}}^{\text{polycryst}} \approx 0.25\chi_{\text{V}}^{\text{iso,cryst}}$, being much larger than $\delta_{\text{BMS}}^{\text{container}}$. In the present work, we used containers with $L/D \approx 4$ for powder samples.

Next, we calculate the effect of a randomly oriented polycrystalline sample on the basis of the model described in the previous section and in the reference (*10*). The lineshape is

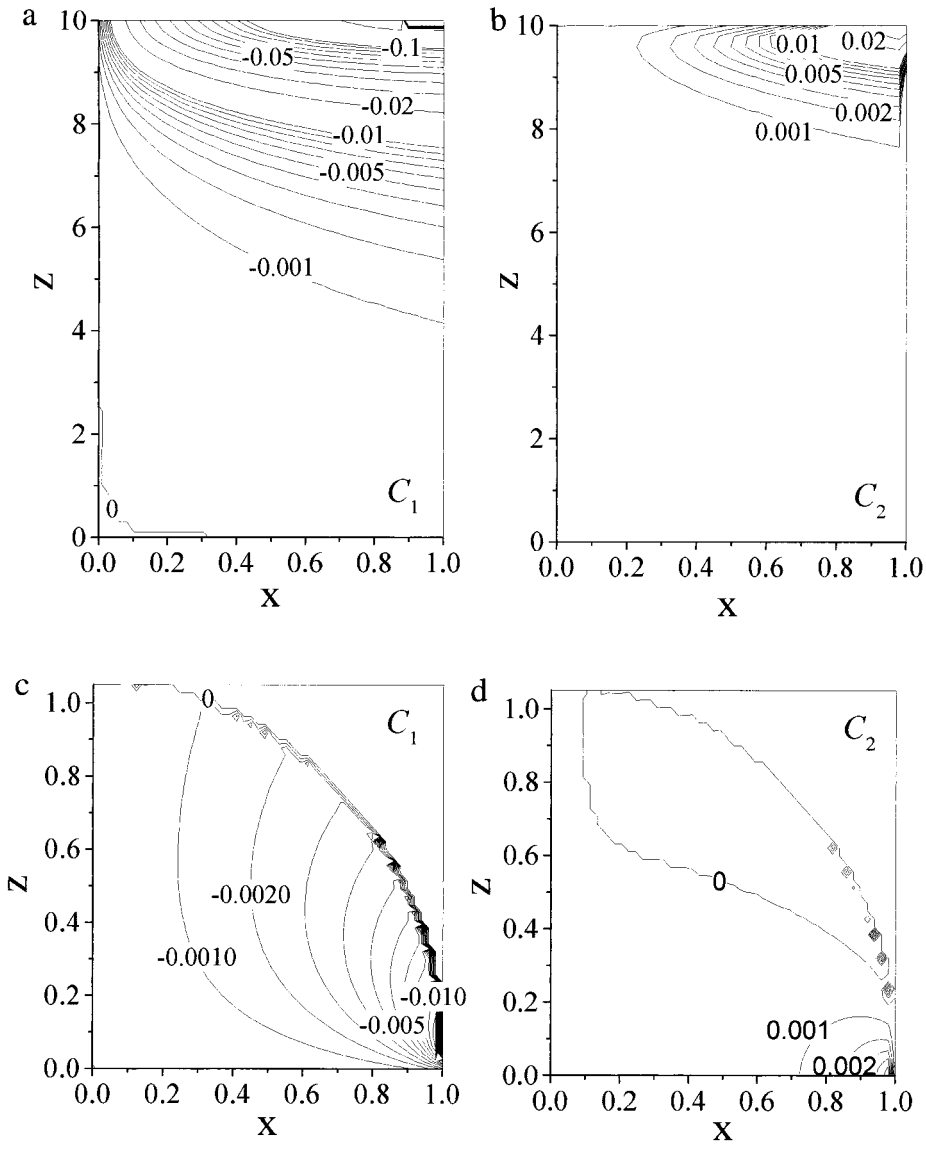

FIG. 2. Calculated distribution of the bulk magnetic susceptibility shift tensor in a cylindrical container with $L/D = 10$ (a, b) and in a spherocylinder with $L/D = 1.05$ (c, d). The coefficients C_1 and C_2 defined by Eq. [14] are shown in (a), (c), and (b), (d), respectively. They were calculated within an xz-plane ($y = 0$), where x and z are the radial and the cylindrical coordinates, and the origin is the center of the container. Only the upper-right quadrant is shown.

assumed to be Gaussian and the FWHM can be obtained from the second moment M_2 by using

$$\mathrm{FWHM} = 2\sqrt{2 \ln 2 M_2}. \qquad [15]$$

When the FCC lattice is assumed to be randomly oriented to the static magnetic field, the second moment is given by

$$M_2^{\mathrm{static}} = V_{\mathrm{cryst}}^{-1} \int_{V_{\mathrm{cryst}}} d\boldsymbol{r}\{[\delta_{11,\mathrm{BMS}}^{\mathrm{polycryst}}(\boldsymbol{r})^2 + \delta_{22,\mathrm{BMS}}^{\mathrm{polycryst}}(\boldsymbol{r})^2 + \delta_{33,\mathrm{BMS}}^{\mathrm{polycryst}}(\boldsymbol{r})^2]/5 + [\delta_{11,\mathrm{BMS}}^{\mathrm{polycryst}}(\boldsymbol{r})\delta_{22,\mathrm{BMS}}^{\mathrm{polycryst}}(\boldsymbol{r}) + \delta_{22,\mathrm{BMS}}^{\mathrm{polycryst}}(\boldsymbol{r})\delta_{33,\mathrm{BMS}}^{\mathrm{polycryst}}(\boldsymbol{r}) + \delta_{33,\mathrm{BMS}}^{\mathrm{polycryst}}(\boldsymbol{r})\delta_{11,\mathrm{BMS}}^{\mathrm{polycryst}}(\boldsymbol{r})]/15\} \qquad [16]$$

where $\delta_{jj,\mathrm{BMS}}^{\mathrm{polycryst}}(\boldsymbol{r})$ ($j = 1, 2, 3$) are the principal values of a tensor $\hat{\delta}_{\mathrm{BMS}}^{\mathrm{polycryst}}(\boldsymbol{r})$. The magnetic susceptibility tensor $\hat{\chi}_{\mathrm{V}}^{j}$ of each crystallite is assumed to be axially symmetric with a random orientation and a common anisotropy. Figure 4a shows the plot of the FWHM scaled by the isotropic susceptibility $\chi_{\mathrm{V}}^{\mathrm{iso,cryst}}$ against a packing probability p and the anisotropy $\Delta\chi = (\chi_{\mathrm{V}\parallel}^{\mathrm{cryst}} - \chi_{\mathrm{V}\perp}^{\mathrm{cryst}})/\chi_{\mathrm{V}}^{\mathrm{iso,cryst}}$. The values for $\Delta\chi = 0$ are quite similar to those reported in Ref. (*10*). In our present calculation, however, the FWHM increases more slowly as $|\Delta\chi|$ increases than that shown in Ref.

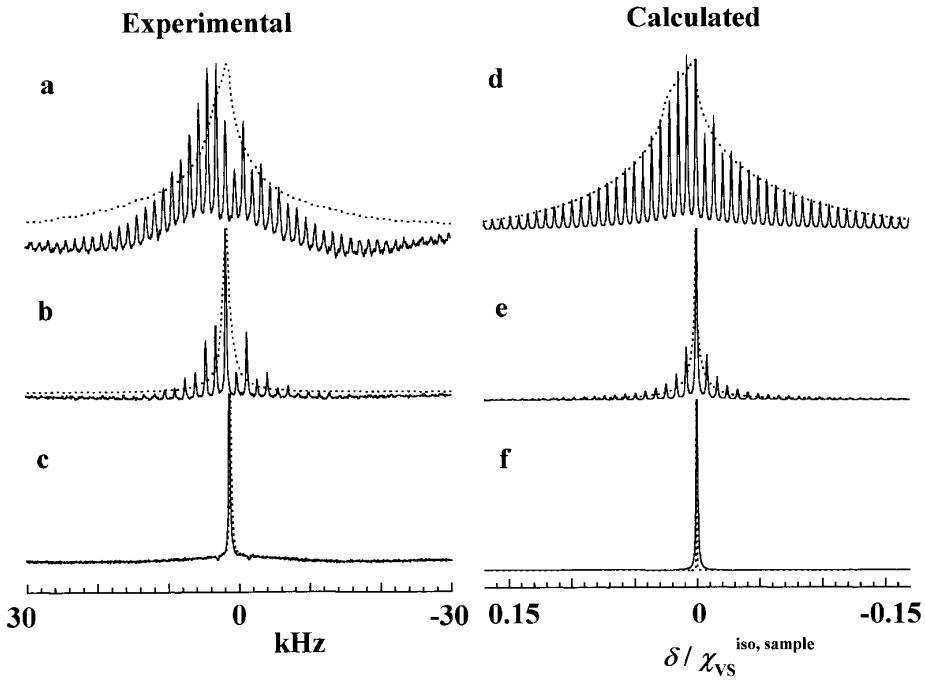

FIG. 3. Effect of a cylindrical sample container on static (⋯) and MAS (—) NMR spectra. (a), (b), and (c) show the ^{1}H NMR spectra of a 1 M water solution of $Dy(NO_3)_3 \cdot 9H_2O$ observed at a resonance frequency of 300.46 MHz in cylindrical containers with a length (L) and a diameter (D) of $L = 3.2$ mm and $L/D = 0.8$ (a), $L = 13.2$ mm and $L/D = 3.3$ (b), and $L = 24$ mm and $L/D = 12$ (c), respectively. The length of the RF coil is about 11 mm. (d), (e), and (f) are the calculated spectra corresponding to the experimental spectra (a), (b), and (c), respectively. The horizontal axis in (d), (e), and (f) represents a BMS shifts scaled by the isotropic volume susceptibility of the sample. The MAS NMR line broadening was given by the Lorentzians lineshape with $T_2 = 1.3$ ms determined by a Hahn echo experiment. The static spectra were calculated without any convolution. The spectra (d) and (e) were calculated by assuming that all the region in the cylindrical container was excited, while the spectrum (f) was calculated by assuming that 50% of the whole region around the center was excited.

(*10*). The difference may arise from the fact that Eq. [12] does not include the contribution of the crystallite which contains the observed nucleus. When p approaches zero, the FWHM also becomes zero, since in this limit there is no crystallite close to the observed one enough to cause any line broadening, and inside a sphere, the demagnetizing field is uniform.

The FWHM of MAS NMR spectra can also be calculated by assuming the Gaussian lineshape from the second moment

$$M_2^{\mathrm{MAS}} = V_{\mathrm{cryst}}^{-1} \int_{V_{\mathrm{cryst}}} d\boldsymbol{r} [Tr\{\hat{\delta}_{\mathrm{BMS}}^{\mathrm{polycryst}}(\boldsymbol{r})\}]^2/9 . \qquad [17]$$

By using Eq. [12] this equation can be rewritten as

$$M_2^{\mathrm{MAS}} = (\chi_{\mathrm{V}}^{\mathrm{iso,cryst}} \Delta\chi/12\pi)^2 V_{\mathrm{cryst}}^{-1} \int_{V_{\mathrm{cryst}}} d\boldsymbol{r} [\sum_j p_j \times \{3[\boldsymbol{\chi}^j \cdot (\boldsymbol{r}_j - \boldsymbol{r})]^2/|\boldsymbol{r}_j - \boldsymbol{r})|^5 - 1/|\boldsymbol{r}_j - \boldsymbol{r}|^3\}]^2, \qquad [18]$$

where $\boldsymbol{\chi}^j$ is the unit vector parallel to the unique axis of $\hat{\chi}^j_{\mathrm{V}}$ with a random orientation. Figure 4b shows the FWHM scaled by $|\chi_{\mathrm{V}}^{\mathrm{iso,cryst}} \Delta\chi|$. The FWHM increases monotonically as the packing probability p increases.

To confirm the validity of the above calculations we have recorded ^{13}C NMR spectra of $Pr(C_2D_5SO_4)_3 \cdot 9H_2O$ and $Yb(C_2D_5SO_4)_3 \cdot 9H_2O$. Figs. 5 and 6 show the static NMR spectra and Figs. 7 and 8 show the MAS NMR spectra. For these samples, the X-ray structural data (*12*) and the magnetic susceptibility data (*13–15*) of single crystals are available. The crystal structure of either compound is $P6_3/m$ with $Z = 2$, and each of the two $[Ln(H_2O)_9]^{3+}$ ions has the $\bar{3}$ axis in parallel to the crystallographic 6_3 axis. Thus, the magnetic susceptibility tensor of each ion is proportional to the macroscopic susceptibility of the crystal when a diamagnetic correction is ignored. These two compounds have different magnitudes of the anisotropy $\Delta\chi$, which are 0.03 and -0.24 for the Pr and the Yb compounds, respectively.

The theoretical spectra that do not include any BMS broadening have been calculated as follows: The paramagnetic dipole shift tensors are calculated by using Eq. [11] and added to the chemical shift tensors taken from literature (*29, 30*). The principal values of the chemical shift tensor are (δ_{11}/ppm, δ_{22}/ppm, δ_{33}/ppm) = (29, 16, 5) for a methyl carbon and (86, 79, 31) for a methylene carbon. The principal axes along the most-shielded directions were assumed to be perpendicular to the C–C–O plane. Those along the least-shielded directions were assumed to be parallel to the C–C bond for the methyl

carbon and to the C–O bond for the methylene carbon. The calculated static NMR spectra of powder samples are shown in Figs. 5a and 6a. Figures 5b and 6b show the spectra also taken account of the ^{13}C–^{2}H dipolar interactions between the directly bonded ^{13}C–^{2}H spins by assuming the dipolar coupling constants of −1.1 kHz and 3.5 kHz for the methyl and the methylene carbons. The spectra (b) were convoluted with the Gaussian lineshapes with some FWHM values, and the results are shown with the experimental spectra in Figs. 5c and 6c. The best fit Gaussian FWHM are 40 and 80 ppm for the Pr and the Yb compounds, respectively.

Next we estimated the theoretical values of the BMS broadening due to the polycrystalline effect. The packing density of either powder sample was estimated to be 0.8 by comparing the weight of water and the sample filled in a rotor. It is slightly larger than the packing density of 0.74 for spheres in a FCC lattice. This larger density of the real powder sample can be explained either by the distribution of the crystallite size or by the nonspherical forms of the crystallites. The theoretical FWHM can be estimated either by using $p = 0.8$ and multiplying a factor of 1/0.74 to $\chi_V^{iso,cryst}$, or by using $p = 1$ and multiplying a factor of 0.8/0.74 to $\chi_V^{iso,cryst}$. These two methods give values for the FWHM of 55 and 32 ppm for the Pr compound and 90 and 54 ppm for the Yb compound, respectively. In our samples, water protons are not deuterated. The FWHM due to the average water proton ^{13}C–^{1}H dipolar couplings were calculated as 20 and 30 ppm for the methyl and the methylene carbons, respectively, at the static magnetic field applied in our experiment. If the frequency-switched decoupling used in the experiments is inefficient and these interactions are retained, the average second moment $(20^2 + 30^2)/2$ ppm^2 must be added to the second moment due to the polycrystalline effect. Then the theoretical values of the FWHM for

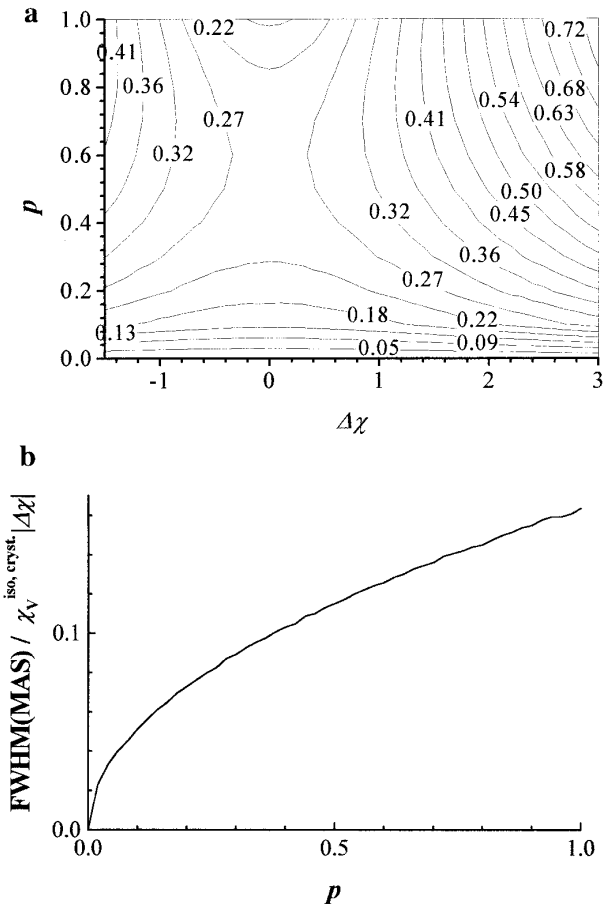

FIG. 4. The calculated FWHM of static and MAS NMR spectra due to the polycrystalline effect. (a) The FWHM of the static spectrum scaled by the isotropic magnetic susceptibility of the crystal, $\chi_V^{iso,cryst}$, is plotted as a function of the packing probability p and the anisotropy of the magnetic susceptibility $\Delta\chi = (\chi_{V\parallel}^{cryst} - \chi_{V\perp}^{cryst})/\chi_V^{iso,cryst}$. (b) The FWHM of the MAS spectrum scaled by $|\chi_V^{iso,cryst}\Delta\chi|$ is plotted as a function of p.

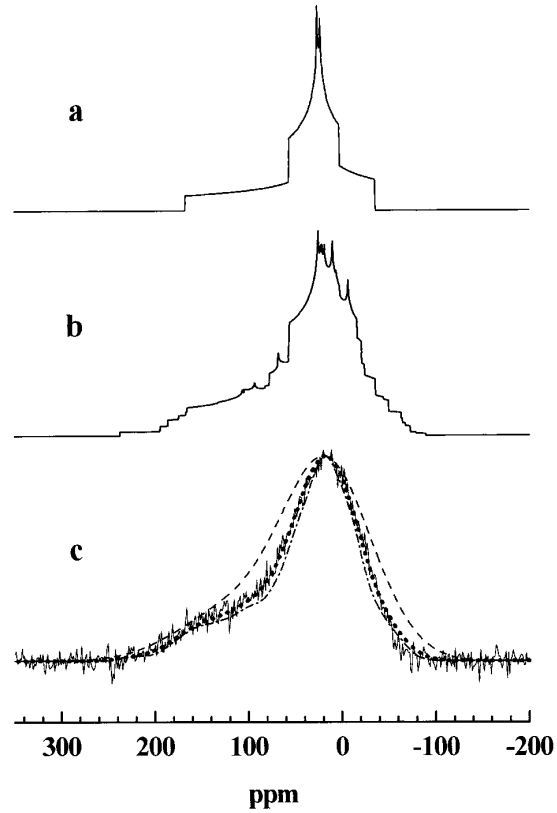

FIG. 5. Comparison of experimental and calculated static ^{13}C NMR spectra of $Pr(C_2D_5SO_4)_3 \cdot 9H_2O$ at the ^{13}C resonance frequency of 75.56 MHz. (a) is calculated by taking account of the chemical shift and the paramagnetic dipolar shift interactions. In addition, the ^{13}C–^{2}H dipolar interactions between the bonded nuclei are included in (b). The solid line (—) in (c) is the experimental spectrum observed by a the frequency-switched ^{1}H decoupling with offset frequencies (−50, 0, 50 kHz), an RF field strength of 60 kHz, and a cycle time of 30 μs. After one decoupling cycle a π-pulse was applied to the ^{13}C spins and the echo signal was observed; 17,280 free induction decays were accumulated with a recycle delay of 7 s. The probe background signal was recorded by separate scans and was subtracted from the observed spectrum. Gaussian convolutions of the spectrum (b) were calculated with FWHM of 20, 40, and 80 ppm and are shown in (c) by (– · –), (· · ·), and (- - -), respectively.

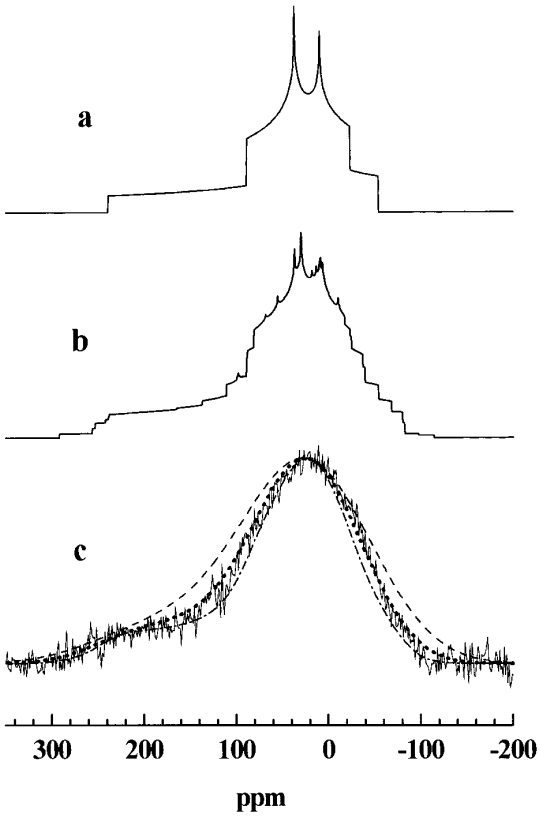

FIG. 6. Comparison of experimental and calculated static ^{13}C NMR spectra of $Yb(C_2D_5SO_4)_3 \cdot 9H_2O$ at the ^{13}C resonance frequency of 75.56 MHz. (a) is calculated by taking account of the chemical shift and the paramagnetic dipolar shift interactions. In addition, the ^{13}C–^{2}H dipolar interactions between bonded nuclei are included in (b). The solid line (—) in (c) is the experimental spectrum observed by the frequency-switched ^{1}H decoupling with offset frequencies (−50, 0, 50 kHz), an RF field strength of 60 kHz, and a cycle time of 30 μs. After one decoupling cycle a π-pulse was applied to the ^{13}C spins and the echo signal was observed; 86,208 free induction decays were accumulated with a recycle delay of 2 s. The probe background signal was recorded by separate scans and was subtracted from the observed spectrum. Gaussian convolutions of the spectrum (b) were calculated with the FWHM of 40, 80, and 120 ppm and are shown in (c) by (–·–), (···), and (- - -), respectively.

$p = 0.8$ and $p = 1$ become 61 and 41 ppm for the Pr compound and 94 and 60 ppm for the Yb compound, respectively. These values are comparable to the experimental values.

We have also recorded ^{13}C MAS NMR spectra for both these compounds and show them in Figs. 7 and 8. We observed the spectra without ^{1}H decoupling because ^{1}H decoupling is known to introduce an extra broadening to MAS NMR spectra (*23*). In the Pr and Yb compounds, the anisotropies of the paramagnetic dipolar shifts of the water protons are very large and have the values of 800–1100 ppm and 1600–1800 ppm, respectively. The spin diffusion among these protons can be suppressed owing to the difference in the principal axis directions of the paramagnetic shift tensors. Thus, the ^{13}C–^{1}H dipolar broadening can be considered as inhomogeneous broadening as pointed out by Raleigh *et al.* (*23*). The effect of these ^{1}H spins on the linewidth of ^{13}C MAS NMR spectra recorded without ^{1}H decoupling can be neglected. In Figs. 7 and 8 the FWHM of the experimental spectra are 1.4 and 1.6 ppm for the methyl and the methylene carbons of the Pr compound, respectively, and 12.5 ppm for both peaks of the Yb compound. The theoretical values were calculated to be 1.0 and 13 ppm for the Pr and the Yb compounds, respectively, and agree very well with the experimental ones. We confirm that Schwerk's model (*10*) modified in this work can predict the BMS line broadening of static and MAS NMR spectra of paramagnetic solids.

CONCLUSIONS

The expression for the BMS shift tensor has been derived by removing the contributions from the Fermi contact shift and the

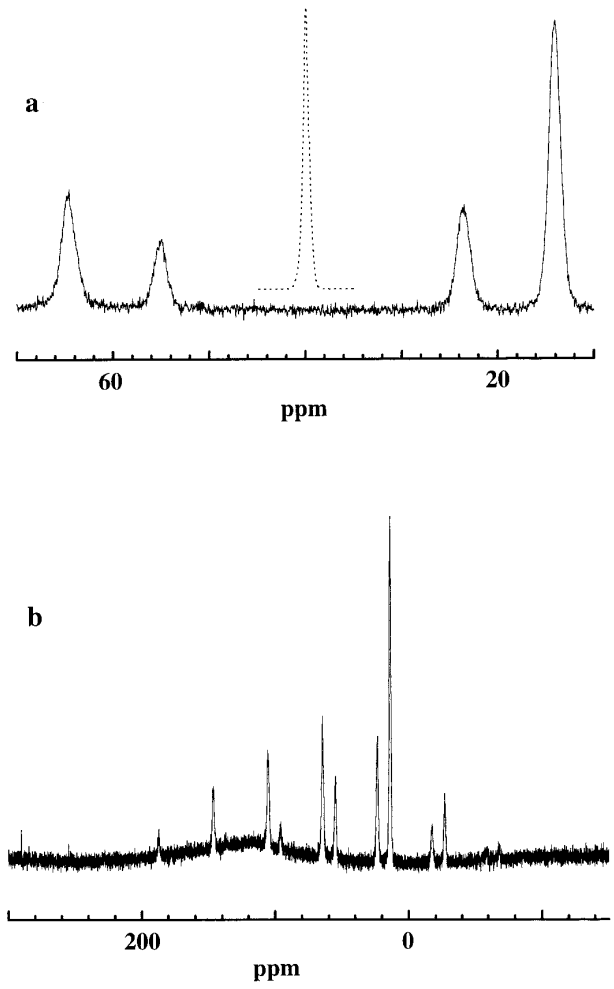

FIG. 7. ^{13}C MAS NMR spectrum of $Pr(C_2D_5SO_4)_3 \cdot 9H_2O$ at the ^{13}C resonance frequency of 75.56 MHz. The spectrum was recorded by a single pulse without ^{1}H decoupling; 5728 transients were accumulated with a recycle delay of 10 s. The dotted line is a spectrum calculated by taking account of the polycrystalline effect. The line position is shifted for appearance. The spinning frequency was 3.1 kHz.

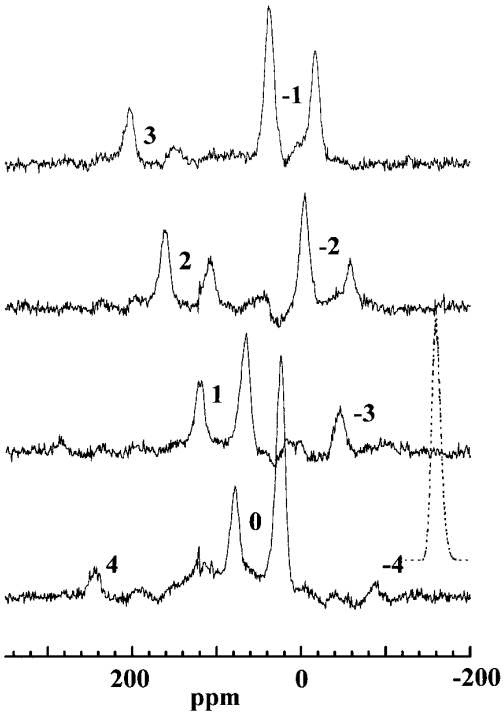

FIG. 8. ^{13}C MAS NMR spectrum of $Yb(C_2D_5SO_4)_3 \cdot 9H_2O$ at the ^{13}C resonance frequency of 75.56 MHz. The spectrum was recorded by a five-pulse PASS sequence (*25*) without ^{1}H decoupling. The spinning frequency was 3.1 kHz; 1024 transients are accumulated for each experiment with a recycle delay of 10 s. The four subspectra show well-resolved sidebands separated by the four multiples of the spinning frequency. The numbers on the spectra show the orders of the spinning sidebands. The dotted line is a spectrum calculated by taking account of the polycrystalline effect. The line position is shifted for appearance.

dipolar shift. The BMS shift due to the random distributions and orientations of crystallites in polycrystalline samples has been calculated by modifying the model proposed by Schwerk *et al.* We eliminated the contribution of the Fermi contact shift from their expression. When the crystallites occupies 80% of a FCC lattice randomly, FWHM of the static and MAS spectra have been calculated as $0.24\chi_V^{iso,cryst}$ (for $\Delta\chi = 0$) and $0.14|\chi_V^{iso,cryst}\Delta\chi|$, respectively. Schwerk's model with our modification has predicted the BMS broadening of the static spectrum and also the ABMS broadening of the paramagnetic lanthanide ethylsulfates very well.

The BMS shifts are also calculated for cylindrical and spherocylindrical sample containers, of which the cylinder axes are directed at the magic angle from the static magnetic field. A long cylindrical container with $L/D = 10$ was found to have a similar magnitude of the BMS shift as a nearly spherical ($L/D = 1.05$) spherocylinder. Since the BMS shift becomes large only near the edge of a cylinder, the BMS shift due to the sample surface can be removed almost completely if we use a long cylinder and excite the spins near the center of the cylinder.

APPENDIX A

The Demagnetizing Tensor for a Cylindrical Sample Container

We assume that the length and the diameter of a cylindrical sample container are given by $L = 2l$ and $D = 2R$, respectively. We use the cylindrical coordinate and express a point on the side plane and a point on the top or bottom plane by $\boldsymbol{r}_S = (R\cos\phi, R\sin\phi, z')$ and $\boldsymbol{r}_S = (\rho\cos\phi, \rho\sin\phi, \pm l)$, respectively, and calculate the demagnetizing tensor $\hat{\nu}(\boldsymbol{r}, S_{cylinder})$ at $\boldsymbol{r} = (x, 0, z)$. The analytical forms of the tensor components are obtained for the integration over z' and ρ (*16*), if we recall that the following integrals can be solved by changing the variable in the integrals from t to θ using $t = a\tan\theta$:

$$\int_{t_0}^{t_1} \frac{dt}{(\sqrt{a^2+t^2})^3} = \frac{1}{a^2}\left\{\frac{t_1}{\sqrt{t_1^2+a^2}} - \frac{t_0}{\sqrt{t_0^2+a^2}}\right\},$$

$$\int_{t_0}^{t_1} \frac{tdt}{(\sqrt{a^2+t^2})^3} = \frac{1}{\sqrt{t_0^2+a^2}} - \frac{1}{\sqrt{t_1^2+a^2}},$$

$$\int_{t_0}^{t_1} \frac{t^2dt}{(\sqrt{a^2+t^2})^3} = \ln\left|\frac{\sqrt{t_1^2+a^2}+t_1}{\sqrt{t_0^2+a^2}+t_0}\right| - \frac{t_1}{\sqrt{t_1^2+a^2}} + \frac{t_0}{\sqrt{t_0^2+a^2}}.$$

The results are given by

$$\begin{aligned}\nu_{xx}(\boldsymbol{r}, S_{cylinder}) - \nu_{yy}(\boldsymbol{r}, S_{cylinder}) &= \frac{R}{4\pi}\int_0^{2\pi} d\phi\, \frac{2R\cos^2\phi - x\cos\phi - R}{R^2+x^2-2Rx\cos\phi} \\ &\times\left\{\frac{(l-z)}{\sqrt{(l-z)^2+R^2+x^2-2Rx\cos\phi}}\right. \\ &\left. + \frac{(l+z)}{\sqrt{(l+z)^2+R^2+x^2-2Rx\,\mathrm{cs}\,\phi}}\right\}, \qquad \text{[A1]}\end{aligned}$$

$$\begin{aligned}\nu_{zz}(\boldsymbol{r}, S_{cylinder}) &= \frac{1}{4\pi}\int_0^{2\pi} d\phi\left\{\frac{l-z}{x^2\sin^2\phi+(l-z)^2}\right. \\ &\times\left[\frac{Rx\cos\phi - x^2 - (l-z)^2}{\sqrt{R^2+x^2+(l-z)^2-2Rx\cos\phi}}\right. \\ &\left.\left. + \sqrt{x^2+(l-z)^2}\right] + \frac{l+z}{x^2\sin^2\phi+(l+z)^2}\right. \\ &\times\left[\frac{Rx\cos\phi - x^2 - (l+z)^2}{\sqrt{R^2+x^2+(l+z)^2-2Rx\cos\phi}}\right. \\ &\left.\left. + \sqrt{x^2+(l+z)^2}\right]\right\}, \qquad \text{[A2]}\end{aligned}$$

$$\nu_{zx}(\boldsymbol{r}, S_{\text{cylinder}}) = \frac{R}{4\pi}\int_0^{2\pi} \cos\phi\, d\phi \left\{ \frac{1}{\sqrt{(l+z)^2 + R^2 + x^2 - 2Rx\cos\phi}} - \frac{1}{\sqrt{(l-z)^2 + R^2 + x^2 - 2Rx\cos\phi}} \right\}, \quad \text{[A3]}$$

$$\begin{aligned}
\nu_{xz}(\boldsymbol{r}, S_{\text{cylinder}}) = {} & \frac{1}{4\pi}\int_0^{2\pi} d\phi \\
& \times \left[\cos\phi \left\{ \ln\left| \frac{\sqrt{R^2 + x^2 - 2Rx\cos\phi + (l-z)^2} + R - x\cos\phi}{\sqrt{x^2 + (l-z)^2} - x\cos\phi} \right| \right.\right. \\
& \left.\left. - \ln\left| \frac{\sqrt{R^2 + x^2 - 2Rx\cos\phi + (l+z)^2} + R - x\cos\phi}{\sqrt{x^2 + (l+z)^2} - x\cos\phi} \right| \right\} \right. \\
& - \left\{ \frac{R\cos\phi\{2x^2\sin^2\phi + (l-z)^2\} - x\sin^2\phi\{x^2 + (l-z)^2\}}{x^2\sin^2\phi + (l-z)^2} \right\} \\
& \times \frac{1}{\sqrt{R^2 + x^2 - 2Rx\cos\phi + (l-z)^2}} \\
& + \left\{ \frac{R\cos\phi\{2x^2\sin^2\phi + (l+z)^2\} - x\sin^2\phi\{x^2 + (l+z)^2\}}{x^2\sin^2\phi + (l+z)^2} \right\} \\
& \times \frac{1}{\sqrt{R^2 + x^2 - 2Rx\cos\phi + (l+z)^2}} \\
& \left. - x\sin^2\phi \left\{ \frac{\sqrt{x^2 + (l-z)^2}}{x^2\sin^2\phi + (l-z)^2} - \frac{\sqrt{x^2 + (l+z)^2}}{x^2\sin^2\phi + (l+z)^2} \right\} \right].
\end{aligned} \quad \text{[A4]}$$

If the cylinder is infinitely long, the demagnetization tensor at $z = 0$ approaches the following:

$$\nu_{xx}(\boldsymbol{r}, S_{\text{cylinder}}) - \nu_{yy}(\boldsymbol{r}, S_{\text{cylinder}}) \rightarrow \frac{R}{2\pi}\int_0^{2\pi} d\phi\, \frac{2R\cos^2\phi - x\cos\phi - R}{R^2 + x^2 - 2Rx\cos\phi}. \quad \text{[A5]}$$

By using the following formula, we can show that this integral is zero inside the cylinder $|x| < R$:

$$\int_0^{2\pi} d\phi\, \frac{1}{1 + a\cos\phi} = \frac{2\pi}{\sqrt{1-a^2}}, \; |a| < 1. \quad \text{[A6]}$$

The other matrix elements also become zero when $z = 0$ and $l \rightarrow \infty$ in Eqs. [A2]–[A4]. The demagnetization tensor inside an infinitely long cylinder is uniform and given by $\nu_{xx} = \nu_{yy} = 1/2$, $\nu_{zz} = 0$ near the center. The BMS shift is given by

$$\delta_{\text{BMS}}^{\text{container}} = \frac{1}{6}(3\cos^2\Theta - 1)\chi_{\text{V}}^{\text{iso,sample}}, \quad \text{[A7]}$$

where Θ is the angle between the static magnetic field and the cylinder axis. When Θ is the magic angle, the shift is zero.

On the top plane of an infinitely long cylinder, $(x\ 0\ z) = (x\ 0\ l)$ and $l \rightarrow \infty$, Eqs. [A1] and [A2] become zero, while Eq. [A3] becomes

$$\nu_{zx}(\boldsymbol{r}, S_{\text{cylinder}}) \rightarrow -\frac{R}{4\pi}\int_0^{2\pi} \frac{\cos\phi d\phi}{\sqrt{R^2 + x^2 - 2Rx\cos\phi}}. \quad \text{[A9]}$$

At the edge of the top plane ($x = R$), this equation is rewritten as

$$\begin{aligned}
\nu_{zx}(\boldsymbol{r}, S_{\text{cylinder}}) &= -\frac{1}{8\pi}\int_0^{2\pi} d\phi\, \frac{\cos\phi}{\sqrt{(1-\cos\phi)/2}} \\
&= -\frac{1}{4\pi}\int_0^{\pi} d\phi \frac{1 - 2\sin^2(\phi/2)}{\sin(\phi/2)} \\
&= -\infty.
\end{aligned} \quad \text{[A10]}$$

The coefficient C_1 diverges near the edge of a cylinder.

APPENDIX B

Antisymmetric Part of a Demagnetizing Tensor

The antisymmetric part of a demagnetizing tensor is given by

$$\nu_{\alpha\beta}(\boldsymbol{r}, S) - \nu_{\beta\alpha}(\boldsymbol{r}, S) = (1/4\pi)\int_S |\boldsymbol{r}_S - \boldsymbol{r}|^{-3}[(\boldsymbol{r}_S - \boldsymbol{r}) \times d\boldsymbol{a}(\boldsymbol{r}_S)]_\gamma, \quad \text{[B1]}$$

where $(\alpha, \beta, \gamma) = (x, y, z), (y, z, x), (z, x, y)$. We show that the integral in Eq. [B1] is zero when it is calculated over a closed surface. When the origin is chosen at an observed position $\boldsymbol{r} = 0$, this equation becomes

$$\nu_{\alpha\beta}(\boldsymbol{r}, S) - \nu_{\beta\alpha}(\boldsymbol{r}, S) = (1/4\pi)\int_S r_S^{-3}[\boldsymbol{r}_S \times d\boldsymbol{a}(\boldsymbol{r}_S)]_\gamma. \quad \text{[B2]}$$

We introduce the polar coordinate system and express the vector $\boldsymbol{r}_S$ as follows:

$$\boldsymbol{r}_S = (r_S\sin\theta\cos\phi, r_S\sin\theta\sin\phi, r_S\cos\theta) \equiv r_S(\theta, \phi)\boldsymbol{e}_3(\theta, \phi). \quad \text{[B3]}$$

The surface vector $d\boldsymbol{a}$ is given by

$$\begin{aligned} d\boldsymbol{a} &= d\theta d\boldsymbol{r}_S/d\theta \times d\phi d\boldsymbol{r}_S/d\phi \\ &= [dr_S/d\theta \boldsymbol{e}_3 + r_S \boldsymbol{e}_1] \times [dr_S/d\phi \boldsymbol{e}_3 + r_S \sin\theta \boldsymbol{e}_2] d\theta\, d\phi \\ &= [r_S^2 \sin\theta \boldsymbol{e}_3 - dr_S/d\theta r_S \sin\theta \boldsymbol{e}_1 - dr_S/d\phi r_S \boldsymbol{e}_2] d\theta\, d\phi, \end{aligned} \quad [B4]$$

where

$$\boldsymbol{e}_1 = (\cos\theta\cos\theta, \cos\theta\sin\phi, -\sin\theta), \quad [B5]$$

$$\boldsymbol{e}_2 = (-\sin\phi, \cos\phi, 0). \quad [B6]$$

Equation [B2] can be rewritten as

$$\begin{aligned} &\nu_{\alpha\beta}(\boldsymbol{r}, S) - \nu_{\beta\alpha}(\boldsymbol{r}, S) \\ &= (1/4\pi)\left\{ \int_0^{\pi} d\theta \int_0^{2\pi} d\phi r_S^{-1} (dr_S/d\phi) \boldsymbol{e}_1(\theta, \phi) \right. \\ &\qquad \left. - \int_0^{2\pi} d\phi \int_0^{\pi} \sin\theta d\ \theta r_S^{-1} (dr_S/d\theta) \boldsymbol{e}_2(\phi) \right\}_{\gamma} \\ &= (1/4\pi)\delta_{\gamma,x}\left\{ \int_0^{\pi} d\theta \cos\theta \int_0^{2\pi} d\ \phi \cos\phi (d \ln r_S/d\phi) \right. \\ &\qquad \left. + \int_0^{2\pi} d\phi \sin\phi \int_0^{\pi} \sin\theta\, d\theta (d \ln r_S/d\theta) \right\}_{\gamma} \\ &\quad + (1/4\pi)\delta_{\gamma,y}\left\{ \int_0^{\pi} d\theta \cos\theta \int_0^{2\pi} d\phi \sin\phi (d \ln r_S/d\phi) \right. \\ &\qquad \left. - \int_0^{2\pi} d\phi \cos\phi \int_0^{\pi} \sin\theta\, d\theta (d \ln r_S/d\theta) \right\}_{\gamma}. \end{aligned} \quad [B7]$$

Equation [B7] is zero; for example, the first term in Eq. [B7] is calculated as

$$\begin{aligned} &\int_0^{\pi} d\theta \cos\theta \int_0^{2\pi} d\phi \cos\phi (d \ln r_S/d\phi) \\ &\qquad + \int_0^{2\pi} d\phi \sin\phi \int_0^{\pi} \sin\theta\, d\theta (d \ln r_S/d\theta) \\ &= \int_0^{\pi} d\theta \left\{ \cos\theta [\cos\phi \ln r_S]_0^{2\pi} + \int_0^{2\pi} d\phi \sin\phi \ln r_S \right\} \\ &\quad + \int_0^{2\pi} d\phi \sin\phi \left\{ [\sin\theta \ln r_S]_0^{\pi} - \int_0^{\pi} d\theta \cos\theta \ln r_S \right\} = 0. \end{aligned}$$

ACKNOWLEDGMENTS

T.P.S. would like to thank the Deutsche Forschungsgemeinschaft for financial support.

REFERENCES

1. N. Bloembergen and W. C. Dickinson, *Phys. Rev.* **79,** 179 (1950).
2. W. C. Dickinson, *Phys. Rev.* **81,** 717 (1951).
3. C. H. Durney, J. Bertolina, D. C. Ailion, R. Christman, A. G. Cutillo, A. H. Morris, and S. Hashemi, *J. Magn. Reson.* **85,** 554 (1989).
4. S. N. Hwang and F. W. Wehrli, *J. Magn. Reson. B* **109,** 126 (1995).
5. D. L. VanderHart, W. L. Earl, and A. N. Garroway, *J. Magn. Reson.* **44,** 361 (1981).
6. A. Alla and E. Lippmaa, *Chem. Phys. Lett.* **87,** 30 (1982).
7. S. Ganapathy and R. G. Bryant, *J. Magn. Reson.* **70,** 149 (1986).
8. C. P. Grey, C. M. Dobson, and A. K. Cheetham, *J. Magn. Reson.* **98,** 414 (1992).
9. A. R. Brough, C. P. Grey, and C. M. Dobson, *J. Am. Chem. Soc.* **115,** 7318 (1993).
10. U. Schwerk, D. Michel, and M. Pruski, *J. Magn. Reson. A* **119,** 157 (1996).
11. T. P. Spaniol, A. Kubo, and T. Terao, *J. Chem. Phys.* **106,** 5393 (1997).
12. J. Albertsson and I. Elding, *Acta Crystallogr. Sect. B.* **33,** 1460 (1977).
13. ''Gmelin Handbook of Inorganic Chemistry'' (H. Bergmann, Ed.), System-no. **39,** C8, p. 362, Springer, Berlin (1981).
14. J. Van den Handel, *Physica* **8,** 513 (1941).
15. S. P. Chachra, and A. Mookherji, *Indian J. Pure Appl. Phys.* **7,** 559 (1969).
16. G. Mozururkewich, H. I. Ringermacher, and D. I. Bolef, *Phys. Rev. B* **20,** 33 (1979).
17. D. T. Edmonds and M. R. Wormald, *J. Magn. Reson.* **77,** 223 (1988).
18. L. F. Fuks, F. S. C. Huang, C. M. Carter, W. A. Edelstein, and P. B. Roemer, *J. Magn. Reson.* **100,** 229 (1992).
19. T. M. Barbara, *J. Magn. Reson. A* **109,** 265 (1994).
20. J. D. Jackson, ''Classical Electrodynamics,'' 2nd ed., Chapter 5, John Wiley & Sons, New York (1975).
21. J. Grange, *Cah. Phys.* **127,** 147 (1961).
22. R. A. Fisher, *Rev. Sci. Instrum.* **47,** 1086 (1976).
23. D. P. Raleigh, C. P. Grey, N. Soffe, and C. M. Dobson, *J. Magn. Reson.* **97,** 162 (1992).
24. W. T. Dixon, *J. Chem. Phys.* **77,** 1800 (1982).
25. O. N. Antzutkin, S. C. Shekar, and M. H. Levitt, *J. Magn. Reson. A* **115,** 7 (1995).
26. A. Bax, *J. Magn. Reson.* **65,** 142 (1985).
27. J. L. White, L. W. Beck, D. B. Ferguson, and J. F. Haw, *J. Magn. Reson.* **100,** 336 (1992).
28. A. Abragam and B. Bleaney, ''Electron Paramagnetic Resonance Transition Ions,'' Chapter 5, Oxford Univ. Press, London (1970).
29. A. Höhene, *Chem. Phys. Lett.* **53,** 97 (1978).
30. M. S. Solum, J. C. Facelli, J. Michl, and D. M. Grant, *J. Am. Chem. Soc.* **108,** 6464 (1986).